Numerical Investigation of the Impact of Thermophoresis on the Capture Efficiency of Diesel Particulate Filters

Guillaume Matte-Deschênes, David Vidal, François Bertrand*

URPEI, Chemical Engineering Department, École Polytechnique de Montréal, Montréal, QC, H3C 3A7, Canada

Robert E. Hayes

Department of Chemical and Materials Engineering, University of Alberta, Edmonton, AB, T6G 2G6, Canada

November 13, 2015

Abstract

The present study investigates the impact of thermophoresis on soot capture in the clean cordierite porous wall of a diesel particulate filter (DPF). A three-step numerical model was developed, consisting of: (1) numerically reconstructing a representative volume of the cordierite porous wall, (2) computing gas flow through the porous wall using the lattice Boltzmann method, and (3) predicting of the DPF capture efficiency based on the time-dependent solution of a modified Langevin equation that takes thermophoresis into account. The validity of the approach was verified by carefully comparing the permeability predictions of a reconstructed cordierite porous wall to

*Corresponding author: françois.bertrand@polymtl.ca

data from the literature. The impact of the magnitude and orientation of the thermophoretic force on the capture of soot particles of various sizes under different flow conditions was investigated. The thermophoretic force applied in or against the flow direction significantly affected the particle capture for the highest particle sizes and flow velocity investigated. Our results suggested that thermophoresis can potentially affect soot deposition uniformity in DPFs. Since the thermophoretic force mainly impacted soot capture efficiency in the presence of particle and flow inertia, a dimensionless criterion defined as the product of Stokes and Reynolds numbers is proposed to predict the onset of what can be called thermophoresis-enhanced inertial impaction. While similar results have been reported by others using simple flow geometries, this is the first time, to our knowledge, that this phenomenon is reported for a complex cordierite porous wall.

Keywords: diesel particulate filter, thermophoresis, filtration efficiency, modelling, lattice Boltzmann method

INTRODUCTION

Global demand for diesel fuel has witnessed constant growth in recent decades and is predicted to continue growing for the next two to three decades. One major oil and gas company has even forecast up to 75 % growth in demand over the 2010–2040 period.[1] In addition to the expanding transportation industry, this increase can be explained by the numerous advantages of diesel over gasoline. For example, diesel engines are more efficient, emit less CO_2, and have longer lifespans than gasoline engines. On the other hand, diesel engines emit approximately ten times more particulate matter, i.e. soot, which is harmful both for the environment and human health. The automotive industry introduced diesel particulate filters (DPF) in the 1980s in order

to remove particulates from engine exhaust gas.

The inner structure of a DPF consists of several thousand narrow parallel channels arranged in a checkerboard pattern, with extremities alternately open and closed to force the gas to flow radially through the porous wall, which is commonly made of cordierite or silicon carbide (see Figure 1). The filtration process usually involves a series of cycles. When the filter is clean or freshly regenerated, soot is captured in the porous wall. Eventually, as the wall gets clogged with soot, in-depth filtration is gradually replaced by wall surface filtration until the pressure drop through the wall and the soot filter cake becomes too high. The filter is then regenerated by active means, such as increasing the temperature of the exhaust gas by, for instance, burning additional fuel. Once cleaned, a new filtration cycle starts.

In addition to high filtration efficiency, the main requirements for DPFs are compactness, low back pressure generation, thermal and mechanical resistance, long lifespan, and good regeneration capability. Most of these requirements are contradictory, making the design of an optimal filter quite challenging. Furthermore, in response to increasingly stringent regulations that mandate e.g. a decrease in particulate emissions from 0.1 to 0.0045 g/km over the 1996–2014 period in Europe, the performance of DPFs must be constantly improved, which requires a better understanding of the capture dynamics of soot particles in DPFs.

Initial soot capture inside the inner porous wall of a DPF involves three main mechanisms: diffusion, interception, and inertial impaction. Since the

diameters of the soot particles to be removed range from 18–1000 nm,[2] all three mechanisms usually play a significant role in the capture process. Their respective importance mainly depends on the flow conditions, the porous structure of the filtering medium, and the size of the soot particles. Diffusion is usually the dominant mechanism for particle diameters of 100 nm and less.[3] Interception occurs at larger particle diameters, usually in the 100–800 nm range, when the gas flow streamline brings soot particles within one particle radius of the surface of the filtering medium, resulting in particle impingement on the medium. Lastly, in the case of even larger soot particles and sudden changes in flow direction, particles may also swerve from the streamlines due to inertia, setting them on a collision course with the filtering medium and resulting in inertial impaction.

Given the multi-scale nature of the transport phenomena involved and their interactions, numerical modelling is considered a useful approach for developing an in-depth understanding and for designing better filters. Since the introduction of DPFs in the early 1980s, a large body of numerical investigations have been carried out to study transport and catalytic reaction phenomena, gas flow and back pressure, soot filtration, and thermal stresses at three different length scales inside a DPF: the porous wall, the filter channel, and the entire DPF volume.[4–6] Thorough and comprehensive reviews of the various numerical models, their development over the years, and their validation with experiments can be found in the recent literature.[7,8]

For studying fluid flow through the porous wall of a DPF, researchers have

either used structural data obtained from a porous medium using X-ray tomography[9–12] or applied reconstruction algorithms to recreate virtual porous walls from statistical descriptors of the porous medium, following the works of Torquato et al.,[13–16] and Kikkinides and Burganos.[17] For simulating the flow through such complex porous structures, the lattice Boltzmann method (LBM) has been introduced to this field by Konstandopoulos[18] and Muntean et al.[19] and quickly recognized as the method of choice in this context for determining permeability or pressure drop.[9–12]

To evaluate porous wall capture efficiency and aerosol deposition, researchers have mainly used the single-collector efficiency theory,[3] following the work of Konstandopoulos and Johnson[20] (see Koltsakis et al.[8] for developments made thereafter). More recently, Hayashi and Kubo[21] used a different approach, which consists of numerically determining the soot particle trajectories throughout a porous structure by solving a Langevin-type equation using the solution of the flow field previously computed with the LBM. In addition to the Brownian force, the force balance incorporated the drag force, the gravitational force, and a thermophoretic force. However, Hayashi and Kubo [11] did not study per se the impact of the thermophoretic force on the capture efficiency of the porous structure. In comparison to other phenomena encountered in a DPF, thermophoresis, a phenomenon by which particles in a fluid subjected to a temperature gradient are attracted toward cooler regions, has not been given much attention in the literature.

Experiments conducted on passive regeneration using various catalysts

and low temperatures, and on active regeneration, have however revealed that large temperature gradients can occur inside DPFs.[8,22–25] In particular, Schmidt and colleagues[22] used radial temperature gradients as high as 7000 K/m in furnace experiments. While the effects of these gradients on the combustion of soot particles have been studied,[22] their impact on soot capture has not been thoroughly investigated.

The thermophoretic force is proportional to the temperature gradient, as described by the following equation:

$$\vec{F}_{th} = -3\pi D_p \mu \beta \zeta \delta \vec{\nabla} T \tag{1}$$

where:

$$\beta = \frac{3}{2}\frac{\mu}{\rho_f T} \tag{2}$$

$$\zeta = \frac{1}{1+3Kn} \tag{3}$$

$$\delta = \frac{\lambda_r + \frac{15Kn}{8}}{1+2\lambda_r+\frac{15Kn}{4}} \tag{4}$$

and where T is the temperature, ρ_f is the density of the fluid, μ is the viscosity of the fluid, λ_r is the ratio of the thermal conductivities of the fluid and particles, and Kn is the particle Knudsen number defined as the fluid mean free path λ divided by the particle radius ($D_p/2$).

In addition to Hayashi and Kubo,[21] thermophoretic deposition in different contexts or geometries such as simple channels, surfaces with curvatures, or water-cooled fluidized beds has been studied in the literature.[26–31] For in-

stance, Konstandopoulos and Rosner[26] observed an inertially-enhanced thermophoretic deposition of small particles in the case of boundary layer aerosol flows over surfaces with streamwise curvatures. They reported that the dimensionless parameter governing inertial effects on thermophoretic transport is $St \times Re_x^{1/2}$, where Re_x is the boundary layer Reynolds number. They also suggested that inertia can cause major changes in aerosol deposition rates even when $St \ll 1$ as long as Re_x is large enough. However, to our knowledge, the effect of thermophoresis on particle capture in the porous wall of a DPF has not been well-documented and has never been formally investigated. Given the magnitude of the reported temperature gradients and the DPF cross-section area over which they occur, thermophoresis could have a significant impact on capture dynamics.

The purpose of the present study was to develop a model to predict the capture efficiency of the inner porous wall of a DPF and to assess the impact of thermophoresis. A model based on a three-step procedure was developed, consisting of: (1) reconstructing a portion of the porous wall using the simulated annealing (SA) technique, (2) computing gas flow through the porous medium using the LBM, and (3) computing soot particle trajectories through the wall by solving a modified Langevin equation that takes the thermophoretic force into account. This multi-step approach will be described in detail. The properties of a reconstructed cordierite porous structure and the resulting hydraulic properties predicted by the LBM model will then be compared to data from the literature to assess the validity of the reconstruc-

tion. Lastly, the impact of thermophoresis on DPF capture efficiency as well as the detailed mechanisms of action of thermophoresis on particle capture will be discussed.

METHODOLOGY

Modelling soot particle capture in the cordierite porous wall of a DPF can be divided into three distinct parts, which can be treated separately. In the absence of tomographic data from a cordierite sample, a representative volume of the porous wall can still be reconstructed from experimental statistical structural correlations from the literature. Then, considering that the soot content in the exhaust gas is < 0.001 mL/L, the interaction between the gas flow and the particle trajectories can be treated through a one-way coupling,[32] which consists of computing the air flow using the LBM without taking disturbances from aerosols into account, and using the resulting flow field to calculate the particle trajectories by solving a modified Langevin equation that takes thermophoresis into account. These three steps are described in greater detail in subsequent sections. Lastly, in this section, we provide a description of the numerical experiments performed to determine the impact of thermophoresis on the capture mechanisms.

Reconstruction of the Cordierite Porous Wall

We reconstructed a fragment of a porous cordierite DPF wall using a classical simulated annealing (SA) technique, which belongs to a class of Metropolis algorithms and relies on an energy minimization procedure. It has been chosen over genetic algorithms or the maximum entropy reconstruction technique because it has been reported to be the most precise of the three methods.[33]

With the SA technique, the porous medium to be reconstructed is approximated by a set of voxels, each carrying one of two phases, solid or void. Starting with an initial random phase configuration, the SA technique iteratively inverts the randomly selected voxel phase and verifies whether this makes the new phase configuration more similar to the real medium, which is evaluated by determining the total pseudo-energy of the configuration. The selected algorithm uses a spin-exchange inversion, which means that two voxels of opposite phases are selected at a time and their phases are inverted, unlike spin-flip inversion where only one voxel is selected and its phase flipped. Spin-exchange inversion has the advantage of conserving the exact porosity of the initial configuration.[33] The pseudo-energy of the system is determined by comparing statistical phase correlations of a real sample with those of the medium to be reconstructed.

While one statistical phase correlation can be employed, two are often used to determine the pseudo-energy of a given configuration. Indeed, a two-point correlation is not sufficient to reconstruct a medium with similar hydraulic characteristics to those of the real porous media, because of the

lack of phase connectivity information. Because of this, like others, we combined two-point and lineal-path correlations.[14,33] The two-point correlation function related to a domain Ω is defined as:

$$S(d) = \sum_{\Omega} \frac{\delta_s(d)}{n_t(d)} \tag{5}$$

where $\delta_s(d)$ and $n_t(d)$ are, respectively, the number of pairs of solid voxels and the number of pairs of voxels separated by a distance d. The lineal-path correlation function is defined as:

$$L(l) = \sum_{\Omega} \frac{\omega_s(l)}{n_\Omega} \tag{6}$$

where $\omega_s(l)$ is the number of line segments of length l starting from a specific voxel that fits entirely in the void phase of the medium, and n_Ω is the total number of voxels within the domain Ω. Note that these statistical correlations are calculated using the reference frame orthogonal directions and are considered identical in each of these directions since the medium to reconstruct is isotropic. The total pseudo-energy of a given configuration Ω was thus defined by:

$$E_s(\Omega) = \sum_{d,l} [(S(d) - S_{exp}(d))^2 + (L(l) - L_{exp}(l))^2] \tag{7}$$

where S_{exp} and L_{exp} refer, respectively, to the two-point and lineal-path correlations obtained experimentally from a real fragment of cordierite. The

energy minimization procedure of the SA technique accepts every proposed phase inversion that reduces the current total pseudo-energy of the system (i.e. $\Delta E_s = E_s(\Omega_{after}) - E_s(\Omega_{before}) \leq 0$), while conditionally accepting the ones that increase it with the following probability:

$$P = \exp\left(-\Delta E_s / T_0\right) \tag{8}$$

where T_0 is an arbitrary dimensionless fictitious temperature of the system and ΔE_s is the energy variation generated by the phase inversion. The SA procedure uses fast cooling to increase precision.[14] To reduce the probability of an increase in pseudo-energy toward the end of the reconstruction procedure, which might prevent convergence, the temperature T_0 was taken to be inversely proportional to the number of iterations performed and was chosen such that the probability of conditionally accepting a "bad" inversion is approximately 50 % at the beginning and decreases over time. In the present study, the reconstruction ended when 20 000 inversion attempts were consecutively rejected. A typical value of the energy obtained at the end of the reconstruction procedure was approximately 0.02 compared to ~5 at the beginning. Figure 2 illustrates the SA reconstruction procedure.

The statistical phase correlations used here were obtained from a real fragment of cordierite and scanning electron microscopy:[34]

$$S_{exp}(d) = 0.25 \times \exp\left(-103250 \times d\right) + 0.25 \tag{9}$$

and:

$$L_{exp}(l) = 0.5 \times \exp\left(-61972 \times l\right) \tag{10}$$

The cordierite porous medium had a porosity of 50 % and was discretized using a domain composed of $300 \times 300 \times 300$ voxels with a grid spacing of 1 μm. Initially, the voxels were randomly flagged as solid or void. This domain size was chosen in order to reproduce the real thickness of a cordierite porous wall in a DPF (300μm). Since the positions of the solid voxels were only governed by mathematical functions and were not constrained by physics, it was possible for one voxel or a small group of voxels ($\leq$ 200 voxels) to be isolated and not connected to the rest of the solid phase, especially when close to the boundaries of the domain. Because of the nonphysical nature of these small groups of voxels, they were filtered out of the medium, although the impact of this filtering was negligible both visually and in terms of porosity. The final porosity was 50.29 % $\pm$ 0.02 % for all the reconstructed domains, which was acceptably close to the 50 % porosity target.

Simulation of Air Flow through the Porous Wall

Once a representative volume of cordierite is reconstructed, the flow of a gas through it can be computed using the LBM, which is the method of choice for simulating flows through complex porous media.[35] The flow field obtained was used to determine the hydraulic permeability of the porous medium and to calculate the soot particle trajectories.

Unlike conventional CFD methods that solve the Navier-Stokes equations directly, the macroscopic flow behaviour is recovered by the LBM from a mesoscopic representation of the fluid. Formally, the LBM involves the discretization of the Boltzmann equation in space ($\vec{x}$), velocity ($\vec{e}$), and time (t). The Boltzmann equation from the kinetic gas theory describes the evolution of the probability distribution function of a fluid particle, denoted $f(\vec{x}, \vec{e}, t)$, based on its microdynamic interactions, i.e. propagation and collisions with other particles.

In the LBM, the probability distribution function $f(\vec{x}, \vec{e}, t)$ is represented by particle populations. Discrete populations of particles, denoted $f_i(\vec{x}, t)$, propagate and collide at every time step Δt on a discrete Cartesian lattice, with spacing Δx, and along n_d velocity directions $\vec{e}_i$, where $i = \{1, ..., n_d\}$ and n_d is the number of discrete directions considered. We used a D3Q15 lattice, i.e. a 3-D lattice with $n_d = 15$ velocity directions.[36] At each iteration, $f_i(\vec{x}, t)$ moving in direction $\vec{e}_i$ at position $\vec{x}$ and time t was updated using the following expression:

$$f_i(\vec{x} + \vec{e}_i \Delta t, t + \Delta t) = f_i(\vec{x}, t) + \Omega_{coll}[f_i(\vec{x}, t)] \tag{11}$$

where $\Omega_{coll}[f_i(\vec{x}, t)]$ is the collision term. Particle collisions were modelled using the Bhatnagar-Gross-Krook approximation,[37] which is a simple approximation of relaxation to local equilibrium. The collision term Ω_{coll} in

Equation (11) is given by:

$$\Omega_{coll}[f_i(\vec{x},t)] = \frac{f_i(\vec{x},t) - f_i^{eq}(\vec{x},t)}{\tau} \tag{12}$$

where $f_i^{eq}(\vec{x},t)$ is the equilibrium particle population (see Succi[37] for a detailed expression) and τ is the dimensionless relaxation time that is related to fluid viscosity μ and density ρ:

$$\tau = 3\frac{\Delta t}{\Delta x^2}\frac{\mu}{\rho} + \frac{1}{2} \tag{13}$$

Local density ρ and macroscopic fluid velocity $\vec{u}$ were obtained, respectively, from the particle populations:

$$\rho(\vec{x},t) = \sum_{i=1}^{15} f_i(\vec{x},t) \tag{14}$$

and:

$$\vec{u}(\vec{x},t) = \frac{1}{\rho}\sum_{i=1}^{15} f_i(\vec{x},t)\vec{e}_i \tag{15}$$

Starting from initial conditions and using appropriate boundary conditions, the LBM scheme described in Equation(11) was stepped in time until convergence was reached. The LBM scheme is explicit, which means the population update at a given lattice node is a local operation since it only requires the populations of the immediate neighbouring nodes. This makes it well-adapted to distributed parallelization.

Table 1 summarizes the LBM numerical parameters used for our simu-

lations performed with the parallel workload balanced and memory efficient LBM implementation described elsewhere.[36] Three classical boundary conditions for porous media were used. First, the boundary conditions at the periphery of the domain were periodic, which means that any outgoing population re-enters the domain on the opposite side. Second, to impose a pressure drop in a given $\vec{e}_j$ direction, a body force pointing in this direction was added to each population pointing in a direction not normal to $\vec{e}_j$. Combined with periodic boundary conditions, this "trick" adequately enforces the prescribed pressure gradient.[38] Third, the no-slip wall boundary conditions on the inner solid surfaces of the porous domain were modelled using the classical half-way bounce-back rule, which reflects any incoming populations to the wall in the opposite direction at the next iteration.[37]

This scheme led to the solution of the transient incompressible Navier-Stokes equations up to a second-order truncation error in the limit of low Knudsen and Mach numbers, i.e. for $Kn \ll 1$ and $Ma \ll 1$. For more information on LBM fundamentals and developments, the reader is referred to the textbooks by Guo and Shu,[39] Kremer,[40] and Succi.[37]

Once the flow field is obtained, the medium hydraulic permeability can be evaluated using Darcy's law. To determine the full permeability tensor, three flow simulations per medium are performed by sequentially applying a pressure drop in each of the three directions of the reference frame.[11] In particular, this allows the isotropy of the reconstructed media to be verified.

Lastly, the porous wall and the gas flow were considered to be in ther-

mal equilibrium and while large temperature gradients can occur in a DPF (about several thousand K/m), we assumed the effect of local temperature variation on the flow field to be negligible. Simulations in a simple channel using COMSOL Multiphysics® modelling software indicated that such temperature gradients would increase the mean flow velocity by <1 %, which is not surprising given that the actual temperature variation through a 300-μm thick cordierite wall is only about 2 K. However, these temperature gradients might have a more significant impact on sub-micron aerosol trajectories due to thermophoresis. The methodology used to verify this point is examined next.

Determination of Aerosol Trajectories and Capture

If gravity and electrostatic interactions with the porous wall are ignored, the trajectories of soot particles in the flow can be computed by integrating a Langevin equation that takes drag (a deterministic process) and Brownian motion (a stochastic process) into account:

$$m\frac{d\vec{v}}{dt} = \gamma m\left(\vec{u} - \vec{v}\right) + \vec{\Gamma} \tag{16}$$

where:

$$\gamma = \frac{3\pi D_p \mu}{m c_c} \tag{17}$$

and where $\vec{v}$ is the aerosol particle velocity, m is the aerosol mass, $\vec{\Gamma}$ is the Langevin force for the Brownian effects, and c_c is the Cunningham's slip

correction factor defined as:[41]

$$c_c = 1 + Kn\left(1.142 + 0.558\ exp\left(\frac{-0.999}{Kn}\right)\right) \tag{18}$$

A formal solution for the velocity of the particle is provided by the following equation:[42]

$$\vec{v}(t+\Delta t) = \vec{v}(t)e^{-\gamma\Delta t} + \gamma e^{-\gamma\Delta t}\int_0^{\Delta t} e^{\gamma t'}\vec{u}(\vec{x}(t+t'))dt' + \frac{e^{-\gamma\Delta t}}{m}\int_0^{\Delta t} e^{\gamma t'}\vec{\Gamma}(t+t')dt' \tag{19}$$

We solved this equation using two fourth-order semi-implicit numerical schemes, where the choice of the scheme depended on the stiffness of the problem. When the problem was not too stiff, a classical Runge-Kutta-Cash-Karp scheme was employed. However, when γ became very large compared to the rate of change of the drag force, the problem became stiff and the more robust scheme proposed by Vadeiko and Drolet[42] was used.

It is worthwhile noting that this problem formulation assumed that aerosols are spherical solid particles and that no agglomeration of particles (or conversely, breakage of clusters) takes place. The validity of the last assumption has been verified by Andrews et al.[43] The overall particle trajectory scheme assumed that the aerosols enter the domain upstream from the filter with the same velocity as the fluid. The whole procedure is described in greater detail in Rebai et al.[44]

To take the thermophoretic force (Equation (1)) into account, the follow-

ing modified Langevin equation was used:

$$m\frac{d\vec{v}}{dt} = \gamma m(\vec{u} - \vec{v}) + \vec{\Gamma} + \vec{F_{th}} \tag{20}$$

Obviously, the thermophoretic force is a deterministic contribution to this equation. Based on the same procedure that led to Equation (19), the solution can be expressed as:

$$\vec{v}(t+\Delta t) = \vec{v}(t)e^{-\gamma\Delta t} + \gamma e^{-\gamma\Delta t}\int_0^{\Delta t} e^{\gamma t'}\vec{u}(\vec{x}(t+t'))dt' + \frac{e^{-\gamma\Delta t}}{m}\int_0^{\Delta t} e^{\gamma t'}\vec{\Gamma}(t+t')dt' + \frac{e^{-\gamma\Delta t}}{m}\int_0^{\Delta t} e^{\gamma t'}\vec{F}_{th}(t+t')dt' \tag{21}$$

To solve Equation (21), the aforementioned numerical schemes can be used in a straightforward way. Note that Equation (1) becomes inaccurate for very small particles, i.e. for $D_p < 30$ nm.[45] In addition, because the temperature variation in the domain was relatively small (about 2 K), as discussed in the previous subsection, a constant temperature was used to calculate the Brownian force term in Equation (21).

The efficiency of the filter for capturing aerosol particles with diameter D_{p_i} can be evaluated from their trajectories obtained by solving Equation (21):

$$E_i(D_{p_i}) = \left(1 - \frac{n_{out_i}}{n_{in_i}}\right) \tag{22}$$

where n_{in_i} and n_{out_i} are the numbers of aerosol particles of diameter D_{pi} entering and leaving the filter, respectively. To this end, choosing a D_p value based on the particle size distribution in Figure 3 (approximating the mobility diameters given by Burtscher[2] as equivalent spherical diameters), 22 800 particles were evenly distributed on the domain entry plane upstream from the medium, and their trajectories were computed using a parallel, computationally efficient, code implementation. A particle was considered captured when the distance between the center of the particle and the center of the nearest solid voxel was less than the sum of the particle radius and $\frac{\Delta x}{2}$, i.e. when the particle and the voxel were in contact or overlapped. This "freeze" kind of capture is justified because no or insignificant slippage takes place at the wall and the particles were too small to bounce off the walls.[46] Once captured, the particle was eliminated from the domain, meaning that clogging of the filter was not taken into account. In other words, the filter was considered clean or freshly regenerated.

This procedure was repeated for all D_{pi} values used to discretize the experimental size distribution given in Figure 3. The global efficiency E could then be evaluated using the following equation:

$$E = \sum_i E_i \times p_i \tag{23}$$

where p_i represents the fraction of particles of diameter D_{p_i} in the distribution.

Numerical Experiments

To determine whether thermophoresis has a significant impact on soot particle trajectories and thus on the overall efficiency of a DPF, the orientation of the temperature gradient with respect to the direction of the gas flow through the porous wall was considered. The temperature gradient is oriented radially within the DPF. However, the filter contains several thousand porous walls arranged in a Cartesian checkerboard pattern, creating thousands of possible flow directions with respect to the temperature gradient orientation. To account for this, we studied the four limiting cases presented in Figure 4: (1) the "with" case in which both the thermophoretic force and gas flow point in the same direction, (2) the "against" case in which they point in opposite directions, (3) the "perp" case in which they point in perpendicular directions, and (4) the "without" case in which no thermophoretic force is present. The fourth case served as a reference for evaluating the impact of thermophoresis on capture efficiency.

In addition to the orientation of the thermophoretic force with respect to the flow direction, the impact of the magnitude of both the temperature gradient and the flow velocity on soot capture was investigated for the four cases: three temperature gradients (3500, 7000, and 14 000 K/m), and three superficial gas velocities (0.005, 0.11, and 0.22 m/s, corresponding to average flow rates of 0.0125, 0.275, and 0.55 m^3/s, respectively) were used. The middle range value of 0.11 m/s is a typical velocity usually reported for a DPF.[6,22] Although the temperature gradients and temperature used are larger than

the ones usually encountered during normal gas exhaust filtration operations, they represent a worst-case scenario for the impact of thermophoresis.

In addition, to assess the statistical uncertainty resulting from the stochastic medium reconstruction, the overall simulation procedure was repeated for 7 different reconstructed porous walls. More precisely, 7 media were chosen from 13 reconstructed media based on a selection method proposed by Chaudhuri[47] to ensure statistical representativeness, which was here based on the trace of the permeability tensor of the porous medium and the standard deviation of its diagonal terms.

Tables 2–3 summarize the properties used for the gas and aerosol particles in our simulations. The exhaust gas considered for computing the flow field was air at a constant temperature of 1000 K throughout the 300-μm thick cordierite wall (i.e. close to the temperature reported at the completion of the regeneration process by Bensaid et al.[23]). The soot particles were assumed to be spherical (sizes given in Figure 3) and have the same properties as graphite, regardless of their size. This is of course a simplification, as large particles can be made of loose clusters of smaller ones, in which case properties such as density may change significantly with respect to size. We will return to this in the Results and Discussion section.

Lastly, Table 4 reports corresponding relevant dimensionless numbers. In particular, the calculated (mean) flow Knudsen number (Kn_f) is relatively high due to the large mean free path of air molecules at 1000 K, and thus larger than but close to the limit of $Kn_f = 0.01$ reported in the literature for

the onset of slippage in porous media.[48] Recently, based on flow simulations performed through arrays of staggered and in-line cylinders at 30 % and 50 % porosity using a modified LBM scheme, Miguel[49] reported an increase in permeability attributed to slip for $Kn_f > 0.02$. Consequently, we have assumed in our work that the impact of slippage on the flow field can be neglected. A detailed examination of Knudsen's correction factor[48] showed that even though the local Knudsen number is higher in smaller pores, the resulting slippage effect is not important enough to cause a significant redistribution of the flow.

RESULTS AND DISCUSSION

The presentation of the results is divided into two parts. First, the representativeness of the reconstructed media is assessed with various structural and hydraulic characteristics reported in the literature for cordierite media. Second, the results from the numerical experiments performed to study the impact of thermophoresis on capture efficiency are reported and discussed. In the second part, since all capture efficiency data for the 7 selected media were similar, the results for only one of these media are presented.

Simulations were carried out using up to 16 cores of Compute Canada clusters. The computational time for the reconstruction procedure and the trajectory calculations ranged from 2–3 days, whereas the LBM fluid flow computations required 10 h on average.

Cordierite Medium and Gas Flow Verification

A typical reconstruction of a cordierite porous medium obtained using our implementation of the SA method is presented before (Figure 5a) and after (Figure 5b) filtering out unconnected groups of voxels, as discussed in the Methodology section. Figure 6 shows the simulated flow field obtained for this filtered reconstructed medium using the LBM. Unless mentioned otherwise, the results presented hereafter refer to these filtered media.

Thirteen virtual porous media were reconstructed using the two-point and lineal-path correlations proposed by Vlachos and Konstandopoulos[34] for a cordierite sample of 50 % porosity, and were filtered. As discussed in Methodology section, the 7 media selected had, on average, a 50.3 % porosity and a 16.2-μm pore (Sauter) diameter. An average permeability of $9.60 \pm 0.50 \times 10^{-13}$ m^2 was obtained for the filtered reconstructed media. These values, derived from the LBM flow simulations using Darcy's law, correspond to the mean of the diagonal terms of the permeability tensor averaged over the 7 reconstructed media. Note that the expected isotropy of the media was reasonably well respected since the standard deviation of the three diagonal terms of this tensor was at most ~10 %.

As can be seen in Table 5, these structural and hydraulic properties compare well to the experimental data reported in the literature for various cordierite porous samples with 41.5 % $\leq \epsilon \leq$ 53.7 %. Permeability is a very sensitive hydraulic property with respect to pore size and porosity, and is thus a very suitable quantity for comparing porous media. In order to better

compare our permeability data to results from the literature, the experimental permeabilities were corrected to the same porosity and pore size as those of our virtual reconstructions (Table 5). Our permeability value is very similar to the corrected data reported by Liu et al.[50] and is only about twice as large as other reported values. This relatively small overestimation can be attributed in part to the grid spacing ($\Delta x = 1$ μm) used. Note also that the voxel filtering procedure affected the permeability, since the value obtained for the unfiltered media is $6.71 \pm 0.30 \times 10^{-13}$ m^2, i.e. in even better agreement with the values reported in the literature. Overall, our results indicate that both the reconstruction procedure and the LBM can be used to evaluate soot particle capture.

Aerosol Capture and Impact of Thermophoresis

Figure 7 illustrates the impact of particle size on the trajectories of particles launched from the same location (30 μm upstream from one of the reconstructed media), as calculated by our trajectory algorithm for the highest superficial velocity investigated and in absence of thermophoresis. Three groups of particle trajectories, which relate to the mechanism dominating the motion of the corresponding particles, can be identified: (1) very small particles subject to Brownian motion (trajectories in dark blue shades), which tend to diffuse upstream from the porous medium surface and eventually collide with it; (2) largest particles subject to inertia (trajectories in yellow to red shades), which move more straightforwardly and follow rather loosely

fluid streamlines until they hit the medium surface upon sudden changes of directions; (3) middle-size particles neither subject to inertia nor to significant Brownian diffusion (trajectories in light blue and green shades), which very closely follow fluid streamlines deep into the porous medium. This latter group represents the particles that are expected to penetrate the most. In the case presented in Figure 7, this highest penetration takes place at 0.125–0.250 μm. Note that, as the flow velocity decreases, the trajectories of the large particles become more affected by Brownian diffusion and less by inertia, thus resulting in an increase of the most penetrating particle diameter, as is evidenced in Figure 8.

Aerosol capture efficiencies as a function of aerosol size are presented in Figure 8 for the three flow velocities investigated and for the four cases defined in Methodology section, to assess the impact of the orientation of the thermophoretic force with respect to the flow direction. Let us first focus on the "without" case, i.e. the results with no thermophoretic force. At the two highest flow velocities (Figures 8b–8c), the efficiency curves go through a minimum (corresponding to the most penetrating particle size), which is typical behaviour.[3] This can be explained by the fact that, as discussed in the Introduction, two and sometimes three capture mechanisms may compete, depending on the aerosol size and the fluid velocity: diffusion owing to Brownian motion, interception, and inertial impaction. For the lowest flow velocity (Figure 8a), a monotonic decreasing curve was obtained, meaning that only Brownian diffusion affected capture in the range of aerosol

sizes investigated.

For the three flow velocities examined (with no thermophoretic force), the global capture efficiencies, as calculated by Equation (23), gave 99.3, 96.2, and 94.7 % for increasing flow velocities. This means that the impact of Brownian diffusion decreased when the velocity increased. These predicted global efficiencies were lower than the values provided by DPF manufacturers, which are usually >99.5 % for all aerosol sizes.[51] However, it is important to note that our efficiency values were calculated for a clean (or freshly regenerated) DPF, whereas the manufacturer's values usually correspond to an average value over a whole operating cycle. The clogging of the DPF between two regeneration cycles can drastically improve capture efficiency.

Next, if we focus on the impact of thermophoresis, it can be seen in Figure 8a that at the lowest flow velocity, thermophoresis (whatever its direction with respect to the flow) had no impact on capture efficiency for all aerosol sizes, meaning that Brownian motion was the predominant capture mechanism. For a flow velocity of 0.11 m/s (Figure 8b), a similar conclusion can be drawn except for the largest particle diameters ($D_p > 0.6$ μm), for which small but statistically significant differences appeared between the "with" and the "against" cases, i.e. when the thermophoretic force acts with or against the flow direction. Lastly, at the largest flow velocity (Figure 8c), significant differences appeared for the four cases when $D_p > 0.2$ μm, i.e. when the magnitude of the interception and inertial impaction mechanisms exceeded Brownian diffusion. Interestingly, there was virtually no difference

between the "perp" and "without" cases (when the thermophoretic force was applied perpendicular to the flow direction, and when there was no thermophoresis). This can also be observed for all the results presented hereafter. However, capture efficiency was substantially enhanced in the "with" case, whereas it was lower in the "against" case. This could suggest that the thermophoretic force has the same impact as increasing or decreasing the magnitude of the flow field, whether it acts with or against the flow direction, and that it has no impact when it acts perpendicular to the flow. We will return to this later.

Based on these results, it was possible to estimate the proportion of soot particles that could be affected by thermophoresis in a DPF right after regeneration. Indeed, Schmidt et al.[22] showed that the temperature gradient mainly takes place over a fraction of the DPF cross-section. Wu et al.[52] also showed that soot particles travelling through this region make up 27.4 % of the total number of particles (this fraction was deduced from the results reported in Figures 10–12 of their article for 1000- and 100-nm particles). In our work, for the largest flow velocity (Figure 8c), the data showed that 25.5 % of the total number of soot particles entering the filter are large enough ($D_p > 0.2$ μm) to be affected by thermophoresis. We thus estimated the fraction of particles affected by the thermophoretic force at the highest flow velocity to be approximately 7 % (25.5 % $\times$ 27.4 %) of the total number of particles entering the filter. Note that this fraction of particles represented $\sim$ 27% of the total volume of soot entering the DPF. However, considering

that: (1) the high temperature gradients and the temperature of 1000 K used are more typical of those prevailing during active regeneration or cold start and they are much smaller during normal exhaust gas filtration, and (2) the density of the largest aerosols is probably largely overestimated because they are actually made of loose particle clusters, one would expect that, in regular filtration operation, the volume fraction of soot particles affected by thermophoresis to be much lower than 27 %.

To understand where these particles were captured, the penetration depth in the filter of 0.7-μm particles, i.e. for a particle size that is affected by thermophoresis, is shown in Figure 10 for the highest flow velocity. When the thermophoretic force acted in the flow direction ("with" case), capture was enhanced in the entry region of the filter, whereas the reverse was observed when it acted opposite to the flow ("against" case). The average capture depth for the various aerosol sizes is reported in Figure 9 for the different flow conditions. The impact of the thermophoretic force on capture depth was also only noticeable at the highest flow velocity for $D_p > 0.2$ μm (Figure 9c). Within this diameter range, aerosols were captured as much as 10 μm earlier in the porous structure in the "with" case than in the "against" case, which are the two extremes. While this difference may seem small, it indicates that there is an impact on the transition from deep-bed filtration to soot-cake filtration, i.e. earlier clogging for channels subjected to a thermophoretic force acting in the same direction as that of the flow. Such a change in capture behaviour could lead to asymmetrical deposition between

the opposite walls of the channels right after regeneration, which in turn could affect the regeneration time.[53]

As observed previously in Figure 8c, the impact of thermophoresis on capture efficiency is mainly observed at the highest flow velocity for a range of aerosol sizes (i.e. $D_p > 0.2\ \mu$m), for which interception and inertial impaction are the predominant capture mechanisms. However, the reason for hardly any thermophoresis impact being observed for a flow velocity only twice as small (Figure 8b) is not obvious. To explain this sudden change in behaviour, the capture efficiency data must be analyzed more thoroughly. Figure 11 displays the difference in fractional capture, defined as $\alpha_i = -ln(1 - E_i)$ for each aerosol size,[3] between the "against" and "without" cases as a function of the product of the Stokes (St) and Reynolds (Re) numbers. The quantity $\frac{\alpha_i(\text{“}against''\text{)}-\alpha_i(\text{“}without''\text{)}}{\alpha_i(\text{“}without''\text{)}}$ is thus a measure of the impact of thermophoresis on capture, with a positive value indicating an increase in capture and a negative value a decrease.

The Stokes number, which can be seen as the ratio of the particle inertial forces to the viscous dissipation forces (in the laminar flow regime) is defined here as:

$$St = \frac{\rho_p\ D_p^2\ c_c\ V\ (1-\epsilon)\ S_v}{108\ \mu}\,, \tag{24}$$

where V is the characteristic speed equal to the flow velocity (0.005, 0.11, or 0.22 m/s) and S_v is the specific surface area of the porous medium (which can be related to the Sauter pore diameter by $D = \frac{6}{(1-\epsilon)\ S_v}$). This dimen-

sionless number characterizes the ability of a particle to closely follow a fluid streamline when $St \ll 1$, or to swerve away from a streamline due to inertia at higher Stokes values. The Reynolds number, which represents the ratio of inertial to viscous forces, is defined here as:

$$Re = \frac{6\ \rho\ V}{(1-\epsilon)\ S_v\ \mu} \tag{25}$$

The $St \times Re$ product is thus a combined measure of the magnitude of both flow and particle inertial forces over viscous forces. As such, the larger this product, the more pronounced the impact of inertia on aerosol trajectories.

Figure 11 shows that the impact of thermophoresis was only significant when $St \times Re > 0.0004$ for the three temperature gradients investigated, and that it increased with the value of $St \times Re$ as well as with the magnitude of the temperature gradient. Note that a similar trend was observed with respect to particle capture depth (not shown), as expected. Furthermore, similar conclusions could be drawn from the "with" case. This result suggests that there is a link between inertia and the onset of thermophoretic effects. As mentioned in the Introduction, Konstandopoulos and Rosner[26] found a dimensionless number, $St \times Re^{1/2}$, that governs the onset of inertial effects on thermophoretic transport over surfaces with streamwise curvatures, which is similar to ours. They also suggested that inertia can cause major changes in aerosol deposition rates even when $St \ll 1$ as long as Re is large enough.

Based on all these results, the following mechanism of action for ther-

mophoresis can be established. Within the diffusion regime, thermophoretic effects are negligible with respect to the chaotic motion of aerosols, and consequently, no impact can be detected. Within the interception regime, the Stokes number is small and particles generally flow around obstacles by closely following streamlines (they can only be captured when the distance between the streamline followed and the obstacle is smaller than the particle radius, as mentioned). As the Stokes number increases, soot particles swerve away from streamlines due to an increase of inertia, which more frequently sets them on a collision course with eventual obstacles. This is the inertial impaction regime. In addition to an increase of particle inertia, an increase of fluid inertia, i.e. Reynolds number, leads to the compression of the viscous boundary layer in front of obstacles, resulting in streamlines passing closer to obstacles, thus improving capture. The impact of thermophoresis on soot capture is enhanced by both factors. However, the main reason for particles to swerve away from streamlines stems from a component of the particle velocity towards the obstacle that cannot be cancelled out because of the presence of the thermophoretic force, as highlighted by the force balance of Figure 12. Lastly, the impact of thermophoresis in the presence of inertia explains why the "perp" and "without" cases displayed similar behaviour in the capture efficiency curves shown in Figure 8. Indeed, in the "perp" case, the thermophoretic force is perpendicular to the fluid streamlines. Consequently, when the heat flux goes from the gas towards the solid phase (porous walls), there is an increase in capture, whereas when the heat flux goes from

the solid phase to the gas, there is an equivalent reduction in capture. It is thus reasonable to think that the net effect may be small.

CONCLUSIONS

A computationally efficient three-step simulation model, based on simulated annealing for the reconstruction of the porous wall of a DPF, the LBM for the simulation of air flow through it, and a modified Langevin equation for the computation of particle trajectories, was developed. It shed light on the impact of thermophoresis on soot capture in a cordierite porous wall of a clean (or freshly regenerated) DPF. Permeability predictions of reconstructed portions of a cordierite porous wall which were computed using the LBM agreed closely with data from the literature, confirming the soundness of the approach. From the computed flow field through the cordierite porous wall, the trajectories of soot particles of various sizes were obtained for different operating conditions, and various thermophoresis orientations and magnitudes. Our results showed that applying the thermophoretic force at the highest flow velocity investigated, either with or against the flow direction, can significantly affect particle trajectories, mainly those of particles ranging in size from 0.2–1 μm.

The thermophoretic force impacted soot capture efficiency, mainly in the presence of particle and flow inertia, for a flow regime in which the momentum relaxation time of the particles was not negligible with respect to

the characteristic time of the flow. A dimensionless criterion defined as the product of the Stokes and Reynolds numbers was proposed to predict the onset of what can be referred to as thermophoresis-enhanced inertial impaction. While similar results have been reported in the case of boundary layer aerosol flows over surfaces with streamwise curvatures,[26] this is the first time, to our knowledge, that such a phenomenon has been reported and quantified for a complex cordierite porous wall.

Lastly, even though the impact of thermophoresis was only observed for the highest flow velocity and for "extreme" temperature conditions more representative of those taking place during, for instance, active regeneration or cold start, the proposed dimensionless criterion may serve as a benchmark for gauging the importance of thermophoretic effects. In addition, the magnitude of the impact was shown to depend on the orientation of the thermophoretic force with respect to the flow direction. Given the inherent non-uniform gas velocity distribution within DPFs, thermophoresis could potentially lead to non-uniform soot deposition, which in turn could accentuate flow non-uniformity over time and ultimately affect the regeneration and overall performance of DPFs. The proposed model is a first step towards the development of a multiscale model to predict soot distribution and clogging in a whole DPF. Such a model could serve as a design tool for improving the efficiency of future generations of DPF by, for instance, providing guidelines to make the best use of the thermophoretic force.

ACKNOWLEDGEMENTS

The authors gratefully acknowledge the financial support of the Natural Sciences and Engineering Research Council of Canada and the computer resource allocations provided by Compute Canada.

Nomenclature

c_c	Cunningham correction factor
D	mean pore diameter (m)
D_p	particle diameter (m)
E	capture efficiency
E_s	pseudo-energy
$\vec{F}_{th}$	thermophoretic force (kg·m/s^2)
Kn	particle Knudsen number
Kn_f	flow Knudsen number
L	Lineal-path
L_{exp}	experimental lineal-path
m	aerosol mass (kg)
S	two-point correlation
S_{exp}	experimental two-point correlation
S_v	specific surface (m^2/m^3)
t	time (s)
T	temperature (K)
$\vec{u}$	fluid velocity (m/s)
V	characteristic speed (m/s)
$\vec{v}$	particle velocity (m/s)
ϵ	porosity
$\vec{\Gamma}$	Langevin force (kg·m/s^2)
μ	fluid viscosity (kg/m/s)
ρ	density (kg/m^3)

References

[1] Exxon-mobil (2013) The outlook for energy: A view to 2040, *Tech. Rep.*, Exxon mobil. URL `http://corporate.exxonmobil.com/en/energy/energy-outlook/download-the-report-and-presentation/download-the-outlook-for-energy-report`.

[2] Burtscher, H. (2005) Physical characterization of particulate emissions from diesel engines: a review. *Journal of Aerosol Science*, **36**, 896–932, doi:10.1016/j.jaerosci.2004.12.001.

[3] Hinds, W.C. (2012) *Aerosol technology: properties, behavior, and measurement of airborne particles*, John Wiley & Sons.

[4] Konstandopoulos, A.G., Kostoglou, M., Skaperdas, E., Papaioannou, E., Zarvalis, D., and Kladopoulou, E. (2000) Fundamental studies of diesel particulate filters: transient loading, regeneration and aging. *SAE technical paper*, pp. 01–1016.

[5] Konstandopoulos, A.G. (2000) Deposit growth dynamics: particle sticking and scattering phenomena. *Powder Technology*, **109**, 262–277.

[6] Zhong, D., He, S., Tandon, P., Moreno, M., and Boger, T. (2012) Measurement and prediction of filtration efficiency evolution of soot loaded diesel particulate filters. *SAE Technical Paper 2012-01-0363*, doi: 10.4271/2012-01-0363.

[7] Konstandopoulos, A.G., Kostoglou, M., Vlachos, N., and Kladopoulou, E. (2008) Advances in the science and technology of diesel particulate filter simulation. *Advances in Chemical Engineering*, **33**, 213–294.

[8] Koltsakis, G., Haralampous, O., Depcik, C., and Ragone, J.C. (2013) Catalyzed diesel particulate filter modeling. *Reviews in Chemical Engineering*, **29** (1), 1–61.

[9] Yamamoto, K., Satake, S., Yamashita, H., Takada, N., and Misawa, M. (2006) Lattice boltzmann simulation on porous structure and soot accumulation. *Mathematics and Computers in Simulation*, **72**, 257–263, doi:10.1016/j.matcom.2006.05.021. 2-6.

[10] Tsushima, S., Nakamura, I., Sakashita, S., and Hirai, S. (2010) Lattice boltzmann simulation on particle transport and captured behaviors in a 3d-reconstructed micro porous DPF. *Training*, **2007**, 05–07.

[11] Gao, Y., Zhang, X., Rama, P., Liu, Y., Chen, R., Ostadi, H., and Jiang, K. (2012) Calculating the anisotropic permeability of porous media using the lattice Boltzmann method and x-ray computed tomography. *Transport in Porous Media*, **92**, 457–4726.

[12] Yamamoto, K. and Ohori, S. (2012) Simulations on flow and soot deposition in diesel particulate filters. *International Journal of Engine Research*, **14**, 333–340, doi:10.1177/1468087412456687. 4.

[13] Rintoul, M.D. and Torquato, S. (1997) Reconstruction of the structure of dispersions. *Journal of Colloid and Interface Science*, **186**, 467–476. 2.

[14] Yeong, C. and Torquato, S. (1998) Reconstructing random media. *Physical Review E*, **57**, 495.

[15] Yeong, C. and Torquato, S. (1998) Reconstructing random media. II. three-dimensional media from two-dimensional cuts. *Physical Review E*, **58**, 224. 1.

[16] Manwart, C., Torquato, S., and Hilfer, R. (2000) Stochastic reconstruction of sandstones. *Physical Review E*, **62**, 893–899. URL `http://link.aps.org/doi/10.1103/PhysRevE.62.893`, 1.

[17] Kikkinides, E.S. and Burganos, V.N. (1999) Structural and flow properties of binary media generated by fractional brownian motion models. *Physical Review E*, **59** (6), 7185–7194.

[18] Konstandopoulos, A. (2003) Flow resistance descriptors for diesel particulate filters: Definitions, measurements and testing. *SAE Technical Paper 2003-01-0846*.

[19] Muntean, G.G., Rector, D., Herling, D., Lessor, D., and Khaleel, M. (2003) Lattice-boltzmann diesel particulate filter sub-grid modeling-a progress report. *SAE Technical Papers*, p. 0835. 2003-01.

[20] Konstandopoulos, A. and Johnson, J. (1989) Wall-flow diesel particulate filterstheir pressure drop and collection efficiency. *SAE Technical Paper 890405*.

[21] Hayashi, H. and Kubo, S. (2008) Computer simulation study on filtration of soot particles in diesel particulate filter. *Computers & Mathematics with Applications*, **55**, 1450–1460.

[22] Schmidt, N., Root, T., Wirojsakunchai, E., Schroeder, E., Kolodziej, C., Foster, D.E., Suga, T., and Kawai, T. (2007) Detailed diesel exhaust particulate characterization and DPF regeneration behavior measurements for two different regeneration systems. *SAE Technical Paper 2007-01-1063*.

[23] Bensaid, S., Marchisio, D.L., and Fino, D. (2010) Numerical simulation of soot filtration and combustion within diesel particulate filters. *Chemical Engineering Science*, **65**, 357–363, doi:10.1016/j.ces.2009.06.051.

[24] Valencia, M., López, E., Andrade, S., Iris, M.L., Hurtado, N.G., Pérez, V.R., García, A.G., de Lecea, C.S.M., and López, A.B. (2013) Evidences of the cerium oxide-catalysed DPF regeneration in a real diesel engine exhaust. *Topics in Catalysis*, **56**, 452–456, doi:10.1007/s11244-013-9995-3.

[25] Pidria, M.F., Parussa, F., and Borla, E.M. (2007) Mapping of diesel soot regeneration behaviour in catalysed silicon carbide filters. *Applied Catalysis B: Environmental*, **70**, 241–246.

[26] Konstandopoulos, A.G. and Rosner, D.E. (1995) Inertial effects on thermoporetic transport of small particles to walls with streamwise curvature. *International Journal of Heat and Mass Transfer*, **38** (12), 2305–2315.

[27] Johnson, J.E. and Kittelson, D.B. (1996) Deposition, diffusion and adsorption in the diesel oxidation catalyst. *Applied Catalysis B: Environmental*, **10** (1), 117–137.

[28] Shi, J.P. and Harrison, R.M. (2001) Study of a water-cooled fluidized bed for diesel particle agglomeration. *Powder technology*, **115** (2), 146–156.

[29] Crane, R., Rubino, L., Arcoumanis, C., Golunski, S., McNamara, J., Poulston, S., and Rajaram, R. (2002) Strategies for gasoline particulate emission control - a foresight vehicle project, *Tech. Rep.*, SAE Technical Paper.

[30] Messerer, A., Niessner, R., and Pöschl, U. (2003) Thermophoretic deposition of soot aerosol particles under experimental conditions relevant for modern diesel engine exhaust gas systems. *Journal of Aerosol Science*, **34** (8), 1009–1021.

[31] Ström, H. and Sasic, S. (2012) The role of thermophoresis in trapping of diesel and gasoline particulate matter. *Catalysis Today*, **188** (1), 14–23.

[32] Kittelson, D.B. (1998) Engines and nanoparticles: a review. *Journal of Aerosol Science*, **29**, 575–588.

[33] Patelli, E. and Schuller, G. (2009) On optimization techniques to reconstruct microstructures of random heterogeneous media. *Computational Materials Science*, **45** (2), 536–549.

[34] Vlachos, N.D. and Konstandopoulos, A.G. (2006) Digital materials methods for DPF development, SAE International, SAE Technical Papers, doi:10.4271/2006-01-0260. URL `http://dx.doi.org/10.4271/2006-01-0260`.

[35] Vidal, D., Ridgway, C., Pianet, G., Schoelkopf, J., Roy, R., and Bertrand, F. (2009) Effect of particle size distribution snd packing compression on fluid permeability as predicted by lattice-Boltzmann simulations. *Computers & Chemical Engineering*, **33** (1), 256–266.

[36] Vidal, D., Roy, R., and Bertrand, F. (2010) A parallel workload balanced and memory efficient lattice-Boltzmann algorithm with single unit BGK relaxation time for laminar Newtonian flows. *Computers and Fluids*, **39** (8), 1411–1423.

[37] Succi, S. (2001) *The lattice Boltzmann equation: for fluid dynamics and beyond*, Oxford University Press.

[38] Bertrand, F., Devals, C., Vidal, D., Séguineau de Préval, C., and Hayes, R.E. (2012) Towards the simulation of the catalytic monolith converter using discrete channel-scale models. *Catalysis Today*, **188**, 80–86, doi: 10.1016/j.cattod.2011.12.011.

[39] Guo, Z. and Shu, C. (2013) *Lattice Boltzmann method and its applications in engineering (advances in computational fluid dynamics)*, World Scientific Publishing Company.

[40] Kremer, G.M. (2010) *Interaction of Mechanics and Mathematics: Introduction to the Boltzmann Equation and Transport Processes In Gases*, Springer.

[41] Kulkarni, P., Baron, P.A., and Willeke, K. (2011) *Aerosol measurement: principles, techniques, and applications*, John Wiley & Sons.

[42] Vadeiko, I. and Drolet, F. (2009) A fourth-order algorithm for solving the multi-dimensional kramers equation in Langevin form. *Journal of Physics A: Mathematical and Theoretical*, **42** (31), 315 002.

[43] Andrews, G., Clarke, A., Rojas, N., Gregory, D., and Sale, T. (2000) Diesel particle size distribution changes along a practical exhaust system during cold start in a passenger car IDI diesel. SAE paper 2000-01-0514. daly d (2001) mechanism of soot suppression during diesel combustion by water. *Fuel Chemistry Division Preprints*, **46**, 394–399.

[44] Rebaï, M., Drolet, F., Vidal, D., Vadeiko, I., and Bertrand, F. (2011) A lattice boltzmann approach for predicting the capture efficiency of random fibrous media. *Asia-Pacific Journal of Chemical Engineering*, **6**, 29–37, doi:10.1002/apj.441.

[45] Li, W. and James Davis, E. (1995) Measurement of the thermophoretic force by electrodynamic levitation: microspheres in air. *Journal of aerosol science*, **26** (7), 1063–1083.

[46] Li, A. and Ahmadi, G. (1993) Deposition of aerosols on surfaces in a turbulent channel flow. *International Journal of Engineering Science*, **31**, 435–451. 3.

[47] Chaudhuri, B.B. (1994) How to choose a representative subset from a set of data in multi-dimensional space. *Pattern recognition letters*, **15** (9), 893–899.

[48] Ziarani, A.S. and Aguilera, R. (2012) Knudsens permeability correction for tight porous media. *Transport in Porous Media*, **91**, 239–260.

[49] Miguel, A.F. (2012) Non-darcy porous media flow in no-slip and slip regimes. *Thermal Science*, **16** (1), 167–176.

[50] Liu, Z.G., Skemp, M.D., and Lincoln, J.C. (2003) Diesel particulate filters: Trends and implications of particle size distribution measurement. *SAE transactions*, **112**, 80–93. 4.

[51] Heidelberg, V.H. (2013) *VERT Standards and Procedures for Retrofit to reduce Diesel Engine Emissions*, URL: http://www.epa.gov/international/io/presentations/VERT-Standards.pdf, Moscow, Russia.

[52] Wu, G., Kuznetsov, A.V., and Jasper, W.J. (2011) Distribution characteristics of exhaust gases and soot particles in a wall-flow ceramics filter. *Journal of Aerosol Science*, **42**, 447–461, doi: 10.1016/j.jaerosci.2011.04.003.

[53] Konstandopoulos, A.G., Kostoglou, M., and Housiada, P. (2001) Spatial non-uniformities in diesel particulate trap regeneration. *SAE TRANSACTIONS*, **110**, 609–620.

[54] Fukushima, S., Ohno, K., Vlachos, N., and Konstandopoulos, A. (2007) New approach for pore structure and filtration efficiency characterization. **1999**, 09–27.

[55] Wirojsakunchai, E., Schroeder, E., Kolodziej, C., Foster, D.E., Schmidt, N., Root, T., Kawai, T., Suga, T., Nevius, T., and Kusaka, T. (2007) Detailed diesel exhaust particulate characterization and real-time DPF filtration efficiency measurements during PM filling process, *Tech. Rep.*, SAE Technical Paper, doi:10.4271/2007-01-1063.

[56] Torregrosa, A.J., Serrano, J.R., Arnau, F.J., and Piqueras, P. (2011) A fluid dynamic model for unsteady compressible flow

in wall-flow diesel particulate filters. *Energy*, **36**, 671–684, doi: 10.1016/j.energy.2010.09.047.

Table 1: Numerical parameters used for all LBM simulations. For the convergence criterion, $\|.\|$ represents the Euclidean norm

Parameters	**Values**
Dimensionless relaxation time, τ	1.00
Lattice spacing, Δx (μm)	1.00
Time step, Δt (ns)	1.42
Convergence criterion, $(d\|\vec{u}\|/dt)/(d\|\vec{u}\|/dt)_{max}$	10^{-8}
Initial local fluid velocities, $\vec{u}(\vec{x}, 0)$ (m/s)	$\vec{0}$

Table 2: Properties of the fluid

Property	**Value**
Thermal conductivity (W/m/K)	0.0675
Density (kg/m^3)	0.353
Viscosity (mPa s)	0.0415
Temperature (K)	1000
Pressure (kPa)	101
Mean free path (nm)	275

Table 3: Properties of the particles

Property	**Values**
Thermal conductivity (W/m/K)	119
Density (kg/m^3)	2200
Diameter (nm)	$[18 - 1000]$

Table 4: Properties of the flow

Dimensionless number	**Values**
Flow Knudsen*	0.0170
Particle Knudsen	$[0.298 - 16.5]$
Reynolds	$[6.00 \times 10^{-5} - 2.00 \times 10^{-2}]$
Stokes	$[3.92 \times 10^{-7} - 7.07 \times 10^{-1}]$

* $Kn_f = \frac{\lambda}{D}$ with D taken as the pore Sauter diameter

Table 5: Structural and hydraulic properties calculated from our reconstructed media and reported in the literature for cordierite porous walls

Porosity ϵ (%)	**Pore diameter** D (μm)*	**Permeability** k $\times 10^{13}$(m^2)	**Corrected permeability** k_{corr} $\times 10^{13}$ (m^2)**	**Reference**
50.3	16.2	9.60	9.60	Our media
53.7	17.7	NA	NA	Fukushima et al.[54]
49	13	6.10	9.72	Liu et al.[50]
48.8	12.8	3.96	5.62	Wirojsakunchai et al.[55]
45.7	11.8	2.42	5.02	Wirojsakunchai et al.[55]
45.1	11.8	2.37	4.98	Wirojsakunchai et al.[55]
41.5	12	2.49	5.50	Torregrosa et al.[56]

* Experimental literature data were measured by mercury porosimetry

** Permeability values were corrected for a porosity $\epsilon_{corr} = 50.3$ % and a pore diameter $D_{corr} = 16.2$ μm, using $k_{corr} = k \times \frac{D_{corr}^2}{D^2} \frac{\epsilon_{corr}}{\epsilon}$ derived from the Carman-Kozeny equation[3]

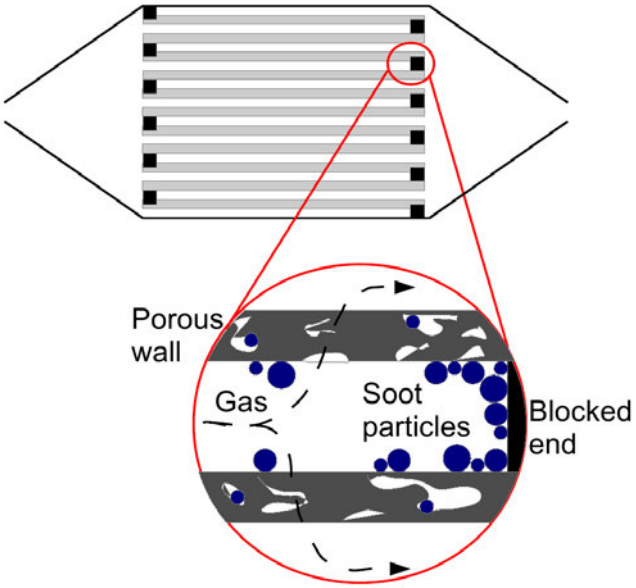

Figure 1: Side view of a DPF with soot capture.

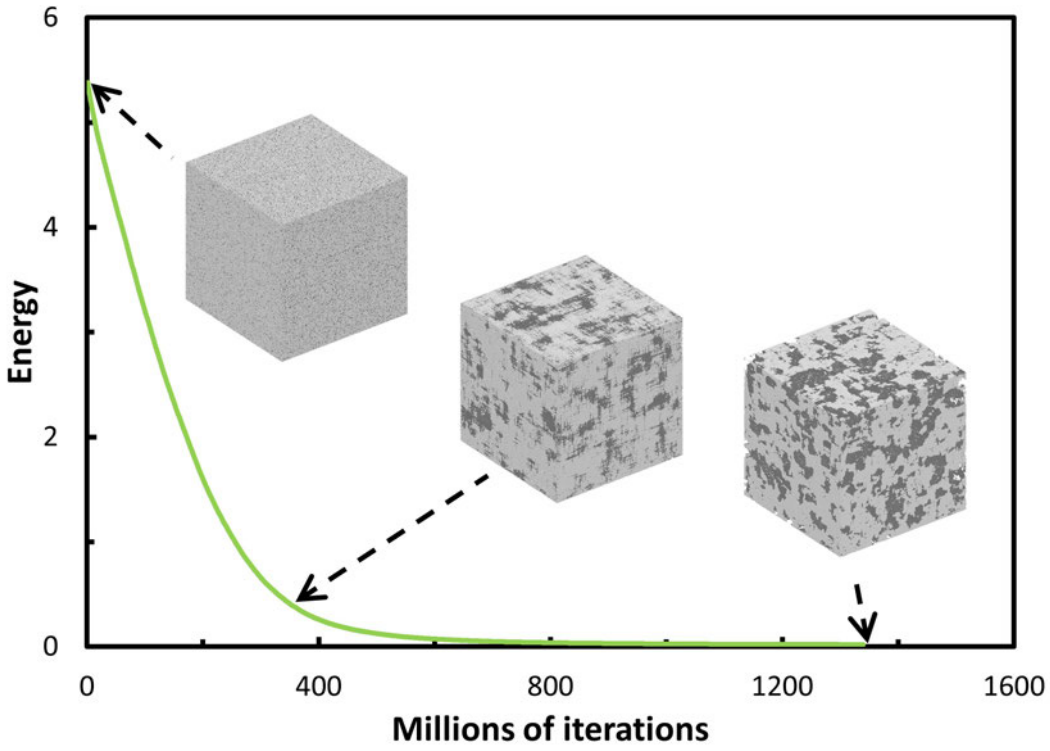

Figure 2: Illustration of the simulated annealing reconstruction procedure.

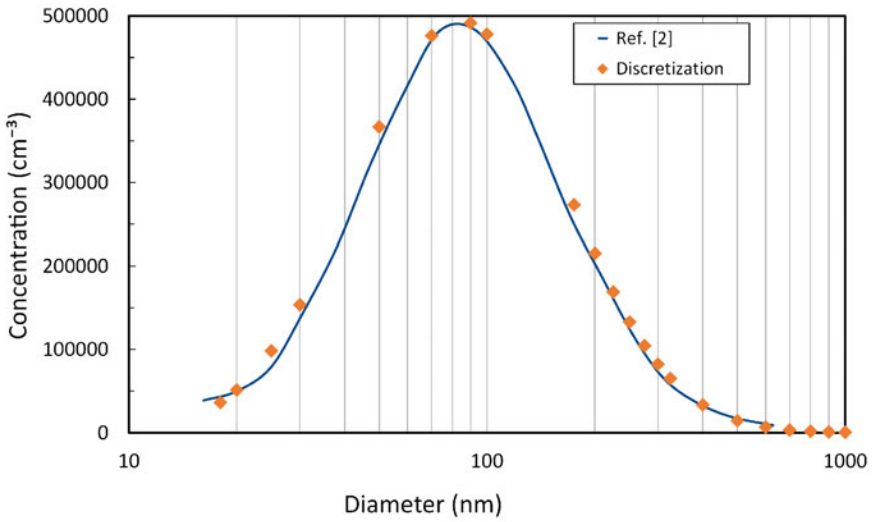

Figure 3: Experimental distribution of soot particle diameters used and discretization.

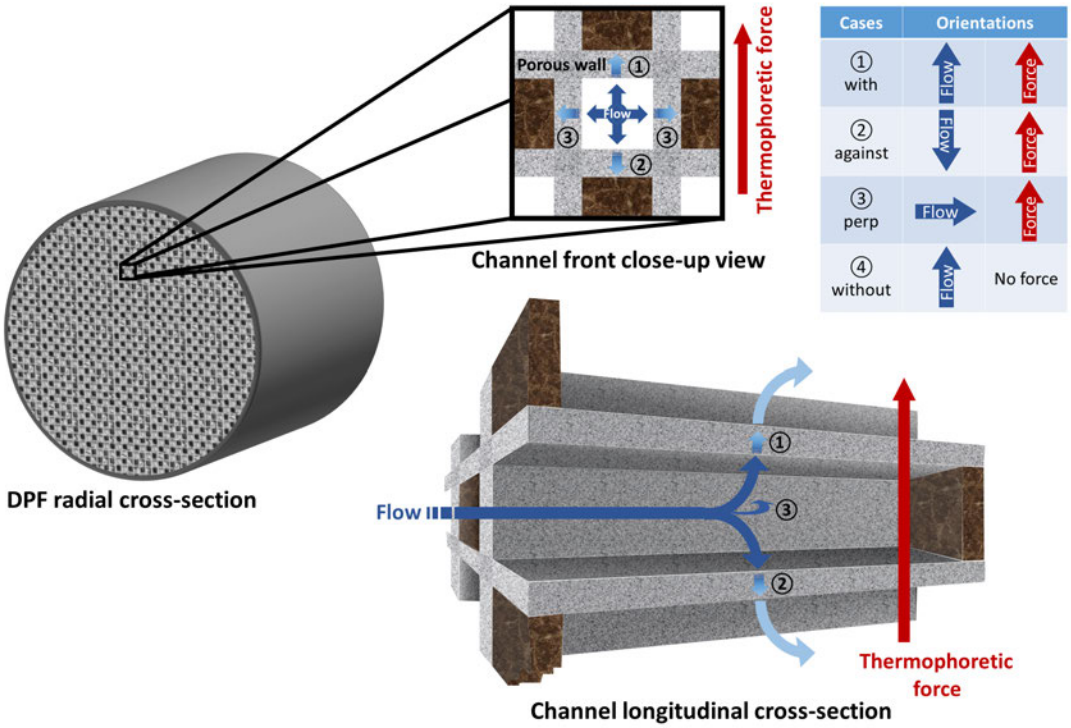

Figure 4: Four cases of thermophoretic force orientation with respect to the direction of the flow. Red arrows indicate the direction of the thermophoretic force, and blue arrows indicate the direction of the flow within the porous wall.

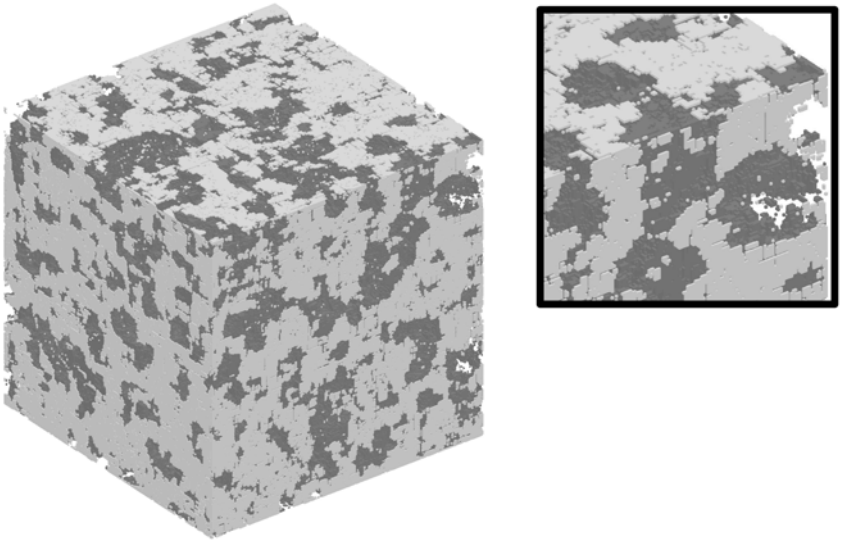

(a)

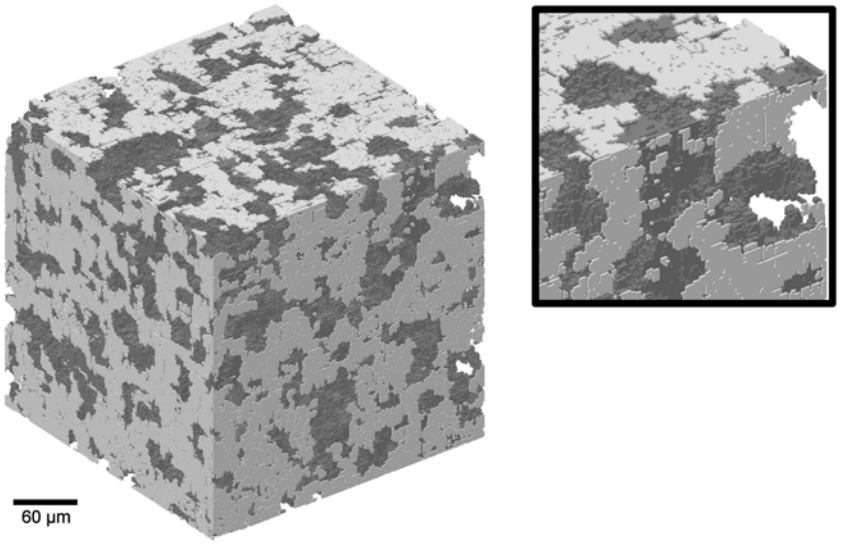

(b)

Figure 5: Example of a reconstructed cordierite porous wall medium before (a) and after (b) filtering out the unconnected voxels (note the unconnected voxels on the top left corner and just below the top right corner in (a)).

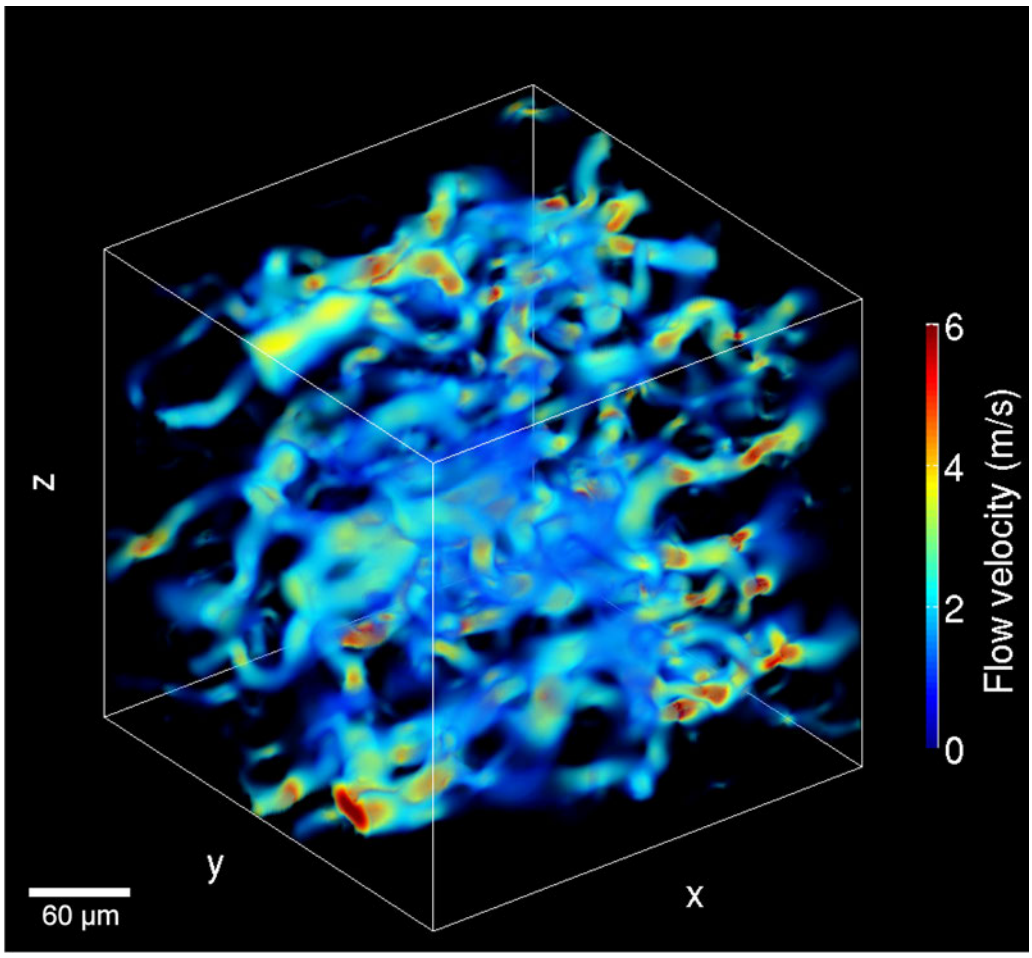

Figure 6: Example of the simulated flow field through the reconstructed medium of Figure 5b for a superficial velocity of 0.22 m/s. The dark blue shades of the colour scale (depicting the lower values of the velocity) have been made transparent to allow a better visualization of flow channeling through the structure.

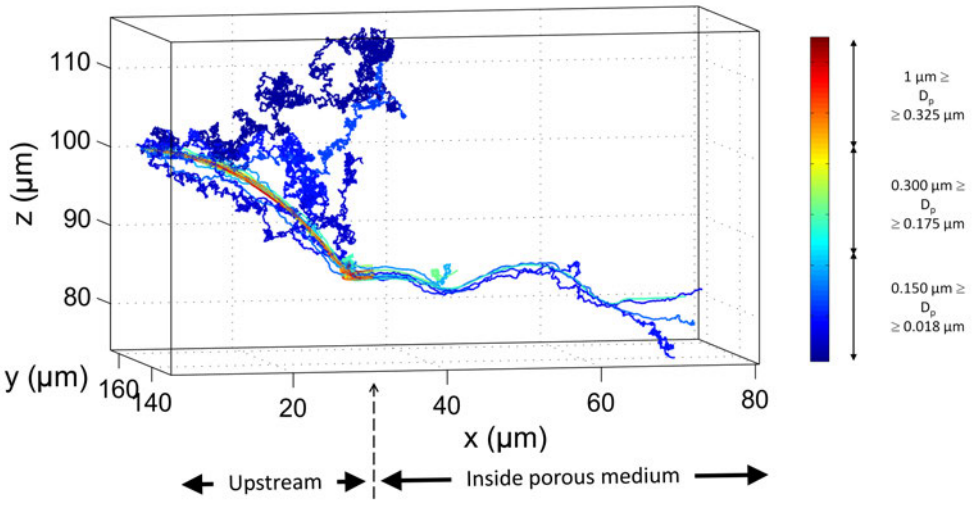

Figure 7: Trajectories for various aerosol diameters computed by our numerical algorithm from a given location slightly upstream from the reconstructed medium (not shown) for a superficial velocity of 0.22 m/s and in absence of thermophoresis. A total of 27 trajectories were computed, split into three equally-sized groups.

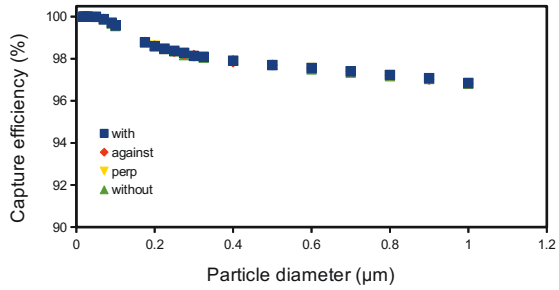

(a) Flow velocity = 0.005 m/s.

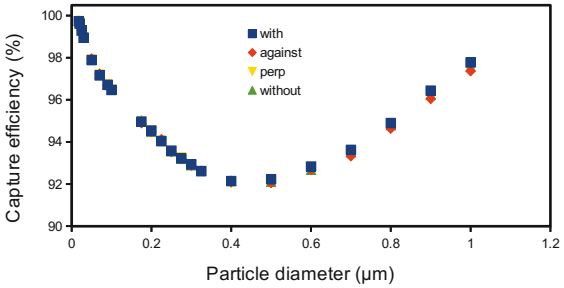

(b) Flow velocity = 0.11 m/s.

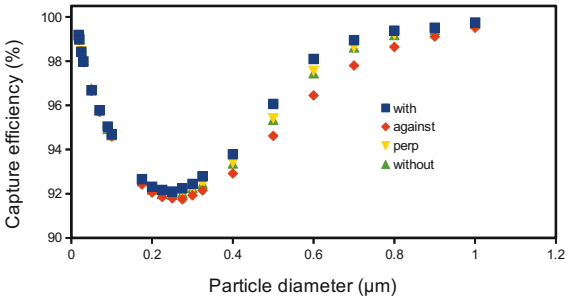

(c) Flow velocity = 0.22 m/s.

Figure 8: Impact of flow velocity and thermophoretic force orientation (for $\|\nabla T\| = 7000\ K/m$) on capture efficiency curves as a function of aerosol size. Error bars are not shown, since they are smaller than the symbols.

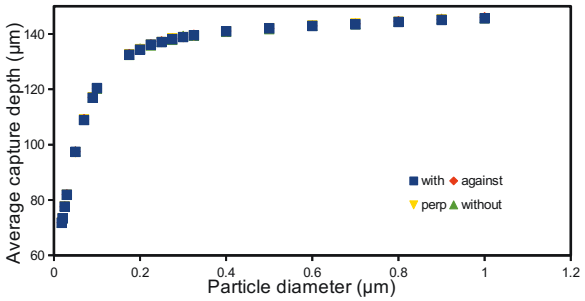

(a) Flow velocity = 0.005 m/s.

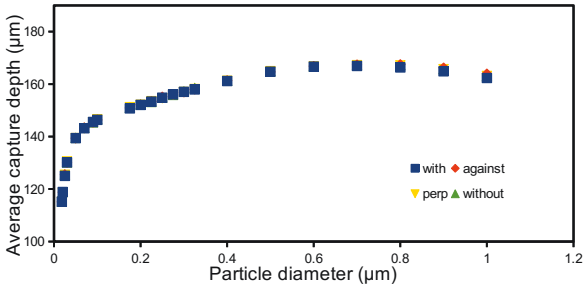

(b) Flow velocity = 0.11 m/s.

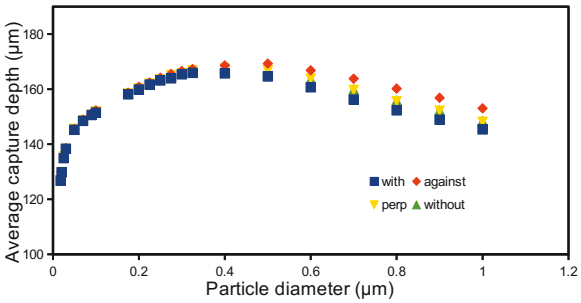

(c) Flow velocity = 0.22 m/s.

Figure 9: Average capture depth as a function of aerosol size for various flow velocities and a temperature gradient of 7000 K/m. Error bars are not shown, since they are smaller than the symbols.

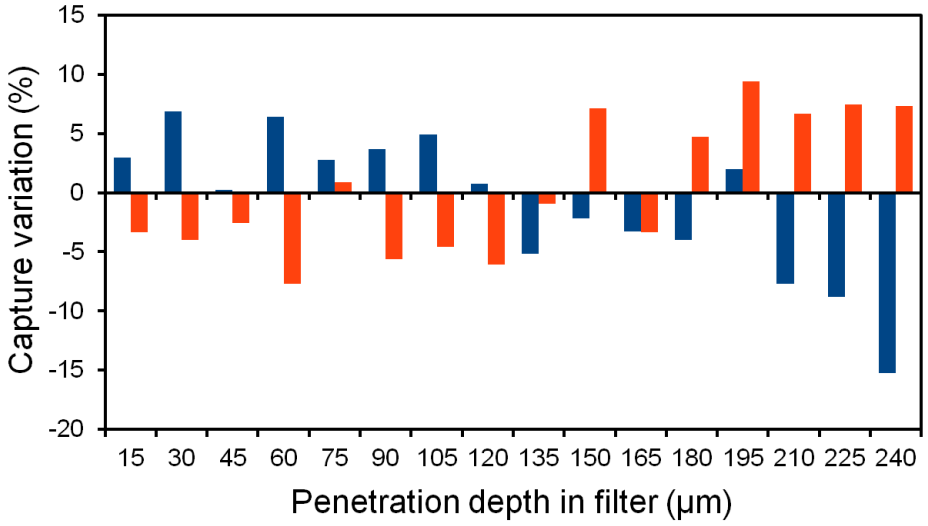

Figure 10: Effect of thermophoresis on particle capture as a function of the penetration depth of 0.7 μm particles in the filter at a flow velocity of 0.22 m/s and a temperature gradient of 7000 K/m, for the "with" (blue) and "against" (orange) cases as compared to the "without" case (reference).

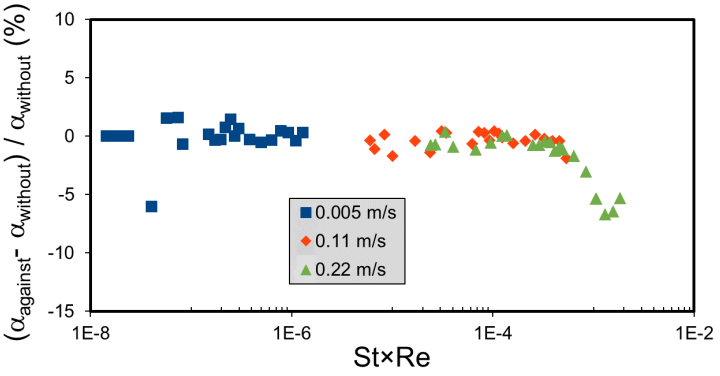

(a) Temperature gradient = 3500 K/m.

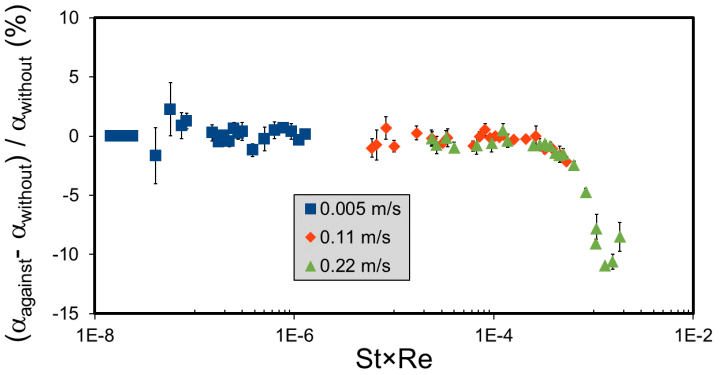

(b) Temperature gradient = 7000 K/m.

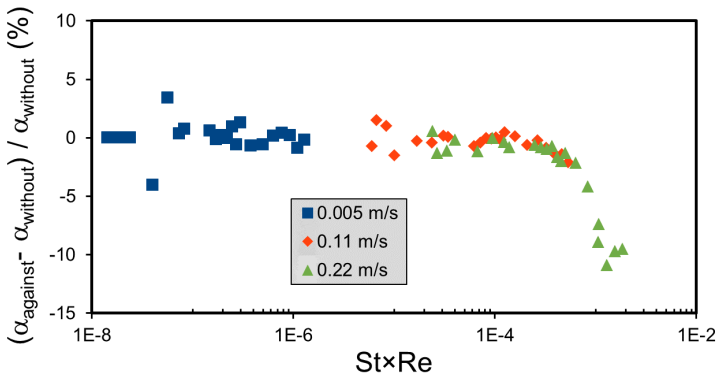

(c) Temperature gradient = 14000 K/m.

Figure 11: Impact of thermophoresis for the "against" case as a function of the magnitude of inertia for three temperature gradients. Blue, orange, and green symbols correspond to flow velocities of 0.005, 0.11, and 0.22 m/s, respectively. Error bars based on standard deviation have only been determined for the middle-range temperature gradient, but are expected to be similar for the other temperature gradients.

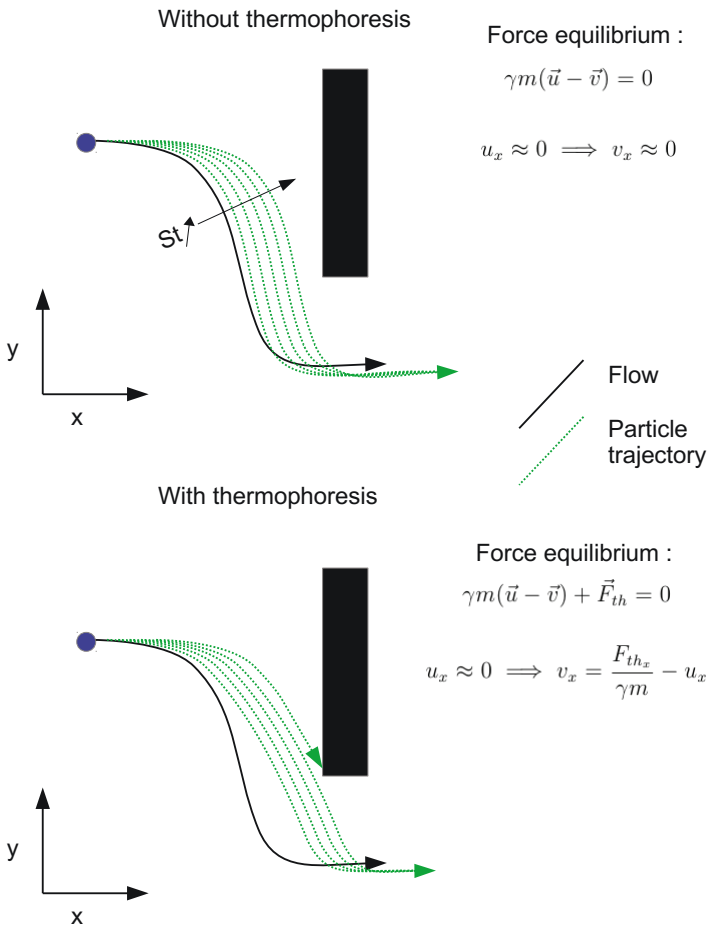

Figure 12: Proposed mechanism of action of thermophoretic force on particle capture. As Stokes number increases, the particle takes a trajectory (in green) closer to the obstacle.